# Optimal 3D single-molecule localization for superresolution microscopy with aberrations and engineered point spread functions

Sean Quirin, Sri Rama Prasanna Pavani, and Rafael Piestun[1]

Department of Electrical, Computer, and Energy Engineering, University of Colorado at Boulder, 425 UCB, Boulder, CO 80309-0425

Photo-activation localization microscopy is a far-field superresolution imaging technique based on the localization of single molecules with subdiffraction limit precision. Known under acronyms such as PALM (photo-activated localization microscopy) or STORM (stochastic optical reconstruction microscopy), these techniques achieve superresolution by allowing only a sparse, random set of molecules to emit light at any given time and subsequently localizing each molecule with great precision. Recently, such techniques have been extended to three dimensions, opening up unprecedented possibilities to explore the structure and function of cells. Interestingly, proper engineering of the three-dimensional (3D) point spread function (PSF) through additional optics has been demonstrated to theoretically improve 3D position estimation and ultimately resolution. In this paper, an optimal 3D single-molecule localization estimator is presented in a general framework for noisy, aberrated and/or engineered PSF imaging. To find the position of each molecule, a phase-retrieval enabled maximum-likelihood estimator is implemented. This estimator is shown to be efficient, meaning it reaches the fundamental Cramer–Rao lower bound of $x$, $y$, and $z$ localization precision. Experimental application of the phase-retrieval enabled maximum-likelihood estimator using a particular engineered PSF microscope demonstrates unmatched low-photon-count 3D wide-field single-molecule localization performance.

computational imaging | nanoscopy | point spread function engineering | pupil encoding | inverse problems

**O**ngoing superresolution microscopy developments are opening up opportunities to explore subcellular structure and function as well as to visualize materials at the nanoscale (1–7). In photo-activated localization microscopy/stochastic optical reconstruction microscopy (PALM/STORM) imaging, random and sparse sets of emitters are allowed to emit independently in time instead of simultaneously, as in normal fluorescence imaging. An image is then formed by the ensemble of precise localization measurements. In this way, the image is not bound by the traditional limit of resolution set by diffraction but rather by the localization precision of the individual molecules. In comparison with other superresolution microscopy techniques (4–6) PALM/STORM is attractive because it enables the recording of multiple single molecules in parallel, with each molecule experiencing limited photo-activation cycles. The technique is also appealing for simultaneously tracking individual molecules over time or measuring the distance between pairs of molecules (8). There is a significant current interest in decreasing the data acquisition time by engineering new fluorescent proteins and organic fluorophores (9) along with optical improvements in photon collection (10, 11). Significant efforts are also underway to reduce systematic errors such as vibrations, drift, and imperfections of the detector (8), as well as bias from asymmetric molecular emission (12). However, existing methods to improve 3D localization use custom estimation algorithms that are not efficient in terms of achieving the fundamental localization limits (13–19).

Therefore the newly discovered frontiers of optical resolution and functionality—such as quantitative tracking and distance measurement—have not been fully realized yet. Optimal 3D localization procedures are critical to increase resolution for a given number of detected photons and to reduce data acquisition time for a given target resolution. Another practical problem is optical aberrations that distort the single-molecule images and negatively affect the localization precision. Accordingly, this paper addresses the problem of optimal 3D localization for arbitrary 3D point spread functions (PSFs) in the presence of noise while providing a solution that rigorously accounts for the inevitable optical system aberrations.

## Current Optical Methods for 3D Single-Molecule Localization

Four main techniques are prevalent in far-field 3D single-molecule localization microscopy: biplane detection (13), astigmatic imaging (14), double-helix (DH) PSF (*Supporting Information* provides an introduction to this topic) (11, 15, 16, 20), and interferometric PALM (10). The first three are of particular interest because they require minor modifications of a standard microscope and operate over relatively long depth ranges (up to 2–3 μm for DH-PSF). In contrast, interferometric PALM offers superb axial resolution but requires more complicated interferometric arrangements and operates over a 200 nm range (10, 21).

To evaluate the performance of each system, the fundamental limit to 3D localization precision can be quantified by means of the Cramer–Rao lower bound (CRLB) (16, 22, 23) (see *Supporting Information* for an introduction to this topic). The CRLB also serves as a benchmark for estimator implementations, by which the realized precision of the estimator should approach this fundamental limit. These uses of the CRLB are increasingly relevant in single-molecule imaging, where the number of photons is inherently limited. Estimators based upon simple geometrical interpretations of the PSF [i.e., centroid (14), rotation angle (11, 15, 16), 2D Gaussian-fit (13–15, 17–19)] have been implemented and are computationally fast but not optimal because they do not reach the fundamental limit of precision for a given physical system. These methods are suboptimal both because of the coarse approximation of the PSF spatial profile and also because of the lack of specific noise statistics.

The inclusion of explicit noise statistics into an estimation algorithm enables the definition of a most-likely 3D position, i.e., a maximum-likelihood estimator (MLE) (24–27). Prior demonstrations of 3D MLEs have only included optical systems that can be described with analytical solutions. This represents a

APPLIED PHYSICAL SCIENCES

limitation for the realizable optical design space that excludes the benefit of numerically optimized solutions. We point to the CRLB analysis demonstrating the 3D performance advantages of one such example, the DH-PSF, relative to the analytical designs as justification for the necessity to include optimized PSFs (22). In addition, existing MLEs do not explicitly address a method for including inevitable experimental aberrations in the optical system. Inclusion of aberrations is critical in 3D methods because microscopes are in principle corrected for aberrations only across a single transverse plane.

Therefore no method has been demonstrated that solves the problems of efficient 3D estimation for generalized optical systems or accurately account for the effects of aberrations induced by both the sample and object. In light of this, here we propose and demonstrate an information-efficient algorithm to achieve the CRLB for 3D localization in the presence of aberrations and using arbitrary PSFs.

## 3D Phase Retrieval (PR) for Optimal Estimation

Optimal estimation requires a faithful model that can be matched to experimental calibration. Unfortunately, a detailed and exhaustive calibration of the PSF at single nanometer shifts, if possible, is not always practical because of the required large data acquisition sets (19, 28), which either become less precise or demand longer calibration times. Hence, we introduce a PR method (29, 30) to accurately recover the 3D PSF at arbitrary coordinates over a continuous 3D domain based on only a few calibration measurements. PR has been used in microscopy to correct aberrations in classical fluorescent imaging using a single-pupil function model (30). This model is an approximation equivalent to a depth-invariant PSF that leads to residual errors even when the vector nature of the fields, the finite size of beads, and noise are taken into account (30). Whereas this approach has been shown to provide good results in conventional (diffraction limited) deconvolution microscopy, its effectiveness is not guaranteed for engineered PSFs and superresolution imaging, where dimensions are one order of magnitude smaller (See *Supporting Information*). Therefore, the PR method proposed here assumes a local, depth-variant model, and is shown below to be effective both for engineered PSFs and for PALM/STORM imaging to improve localization precision and ultimately resolution.

To generate a proper model of the imaging system that accounts for the presence of aberrations and the arbitrary optical system design, a set of calibration images, $\{I_{z1}, I_{z2}, ..., I_{zN}\}$, and a PR algorithm are used to solve for the complex field of the PSF,

$$f_{zn}(x,y) = |\sqrt{I_{zn}(x,y)}|e^{i\varphi_{zn}(x,y)}, \quad [1]$$

with $zn = z1...zN$ indicating $N$ axial positions. A diagram of the PR algorithm demonstrating a working example for estimating the complex field at an arbitrary plane $z_0$ is provided in Fig. 1. For any location of the molecule in space, an accurate model of the PSF is obtained from the images $|f|^2$ by continuously propagating along $\Delta z$ and shifting in $\Delta x$, $\Delta y$ according to the wave equation that governs the evolution of the PSF,

$$f(x,y; \Delta x, \Delta y, \Delta z)$$
$$\propto \mathscr{F}\left\{ \mathscr{F}^{-1}\{f_{zn}\}\left(\frac{u}{\lambda f_{4F}}, \frac{v}{\lambda f_{4F}}\right)e^{i\frac{2\pi}{\lambda f_{4F}}M(u\Delta x + v\Delta y)}e^{-i\frac{\pi}{\lambda}(\frac{u^2+v^2}{f_{4F}^2})M^2\Delta z} \right\}, \quad [2]$$

where $M$ is the magnification, $\lambda$ is the wavelength, and $f_{4F}$ is the focal length of the lens on the image side (see also Fig. 2). The PR algorithm can be implemented using a minimum of two axial positions for calibration images of the PSF, taken at well-known coordinates $\overline{o}_n = \{\Delta x_n, \Delta y_n, \Delta z_n\}$ where $n = 1,2$. However, increasing the number of calibration images for PR has been documented to improve convergence and robustness in the presence of noise (31).



**Fig. 1.** The phase retrieval algorithm for PSF recovery and interpolation. (*A*) A sequence of three local calibration images ($I_{z0-\Delta z}$, $I_{z0}$, $I_{z0+\Delta z}$) is used for recovering the local depth-variant complex amplitude PSF of the optical system that is associated with the aberrated and/or engineered PSF. The search procedure requires five steps (S1–S5) per iteration until a solution converges at plane $z_0$, where the local phase is shown below the intensity image. Comparison of the axial dependence for the experimental and interpolated images of the aberrated DH-PSF are given in panels (*B*) and (*C*), respectively. (*B*) Projections of the experimental images along the $x$ and $y$ axes with axial propagation shows the discrete character of the calibration data. (*C*) The results from the PR algorithm behave smoothly—indicative of proper interpolation of the expected PSF at intermediate image planes to be used for MLE.

Prior methods have assumed that these field estimates can be averaged across the entire depth of focus to provide a best estimate for the system pupil, but this assumption is overly restrictive for high numerical aperture systems as shown in ref. 30, leading to residual errors in the estimated PSFs. Although these errors can be tolerated in applications such as classical diffraction limited deconvolution imaging, without further modifications they could introduce significant errors in localization-based superresolution microscopy (see *Supporting Information*). Therefore, a method that departs from the single-pupil approximation, which implicitly assumes a depth-invariant PSF, is required. It is with this in mind that we implement a depth-variant method, using the PR algorithm with three local and contiguous axial calibration images to find the complex-field at each of the $N$ depth positions. Hence, in this report we assume each estimate to be the best local representation of the associated field and retain this for later use in the MLE.

Knowledge of the absolute value of the amplitude for $f_{z0-\Delta z}$, $f_{z0}$, and $f_{z0+\Delta z}$ is provided from the calibration images as $\sqrt{I_{z0-\Delta z}}$, $\sqrt{I_{z0}}$, and $\sqrt{I_{z0+\Delta z}}$, respectively, and is used to find a unique estimate of $f_{z0}$. Referring to Fig. 1*A*, the propagation of $-\Delta z$ in step S1 is described by a defocus operation to calculate $f_{z0-\Delta z}$, i.e., a shift in object position of $\overrightarrow{o}_{SM} = \{\Delta x = 0, \Delta y = 0, -\Delta z\}$ (see Eq. **2**). After this numerical propagation, the amplitude constraints of $\sqrt{I_{z0-\Delta z}}$ are enforced and the phase component of $f_{z0-\Delta z}$ is kept in step S2 as this represents an improvement in the estimation of this function. This new estimate is then forward-propagated to provide an updated estimate of $f_{z0}$ as step S3. The forward-propagation is continued to $z0 + \Delta z$, the constraints again enforced as step S4, followed by a subsequent back-propagation to the starting point $z0$ to complete the algorithm with step S5. Steps S1–S5 represent a single iteration of the PR algorithm. Iteration continues until a measure of convergence such as the sum-squared-error shows asymptotic behavior. Note that in practice, it has been documented that an optimum $\Delta z$ exists for a given noise level of the calibration images (32). In our experiments, an average of 27 images are taken at each axial position to decrease the noise present in the calibration image (where each axial position is taken at 100 nm intervals). The PR can be further refined—if necessary—using known methods that account for undersampling and broadband emission (33). A generalization of the method presented here is also possible for nonisoplanatic systems.

The result of the PR is a rigorous interpolation of the calibration data that can be used in the MLE process. Note that this process has incorporated the entire optical system into the calibration process without making any significant assumptions about amplitude/phase modulation devices or aberrations. Therefore, optical PSF design and systematic aberrations can be incorporated seamlessly for optimal estimation.

## 3D Maximum-Likelihood Localization Estimation

The optical system description given by the experimental PSF and, if needed obtained via the PR process, is utilized in the second component of this method. Given an experimental image of a single-molecule $I_{exp}$, this optimal estimator searches the object space $\overrightarrow{o}$ for the most-likely PSF match $|f(\overrightarrow{o})|^2$ using Eq. **2**, i.e., the position $\overrightarrow{o}(\Delta x, \Delta y, \Delta z)$ of the molecule that maximizes the likelihood function,

$$\hat{o}(\Delta x, \Delta y, \Delta z) = \arg\max_{\overrightarrow{o} \in \mathbb{R}^3}\{\mathscr{L}(I_{exp}; f(\overrightarrow{o}))\} \qquad [3]$$

Here, $\hat{o}$ is the estimate resulting from the maximization and $\mathbb{R}^3$ is the set of all 3D positions; $\mathscr{L}$ is a function representing the likelihood of the match at $\overrightarrow{o}$ in the presence of noise processes such as Poisson or Gaussian (the Gaussian case is treated in *Supporting Information*).

A proper initial guess accelerates the convergence and avoids local maxima for the optimization required to solve Eq. **3**. Accordingly, the starting axial location $\Delta z^{(1)}$, with (1) denoting the first iteration of the search, is found using the calibration image that best matches the experimental image by minimizing the sum-squared-error of the Fourier coefficient amplitudes (See *Supporting Information*). This results in an initial $z$ estimate that is unrelated to the transverse position of the molecule. The transverse coordinates of the initial estimate $(\Delta x, \Delta y)^{(1)}$, are found separately using a cross-correlation of the experimental image with the previous (best match) calibration image. The maximization in Eq. **3** is then achieved using the iterative update solution (24),

$$o_j^{(p+1)} = o_j^{(p)} - \gamma \left(\frac{\partial^2}{\partial j^2}\mathscr{L}(I_{exp}; f)\right)^{-1} \frac{\partial}{\partial j}\mathscr{L}(I_{exp}; f)\bigg|_{j=o_j^{(p)}} \qquad [4]$$

to find the most-likely match, where $j \in \{\Delta x, \Delta y, \Delta z\}$, $p$ is the iteration number and $\gamma$ is a gain coefficient on the update (expressions for evaluating the derivatives are given in the *Supporting Information*).

## Performance with Simulation Data

The estimation efficiency of this localization method is quantified by simulating a DH-PSF microscope with numerical aperture NA = 1.3 and $M = 91x$, imaging a single molecule with average isotropic emission at $\lambda = 515$ nm. The optical configuration is designed to match that of our typical experimental implementation, as given in Fig. 2 (see also *Supporting Information*). The behavior of the DH-PSF image can be approximately described as a pair of intense lobes that rotate about the mutual center of mass as the object translates axially, shown both in the experimental and PR data of Fig. 1 *B* and *C*, respectively, as well as Fig. 2.

The PR algorithm uses the average of 100 noisy image realizations, taken at three axial positions ($z = -100$ nm, 0 nm, and +100 nm) to form the calibration image set. Note that the PR algorithm can be run initially for system characterization and then store the recovered optical system pupil function for later use to speed up computation time.

The PR-MLE performance is tracked as the number of photons detected from the emitter is varied across a representative range. Poisson noise is considered the dominant noise process, consistent with ideal experimental conditions, with a likelihood function given by,
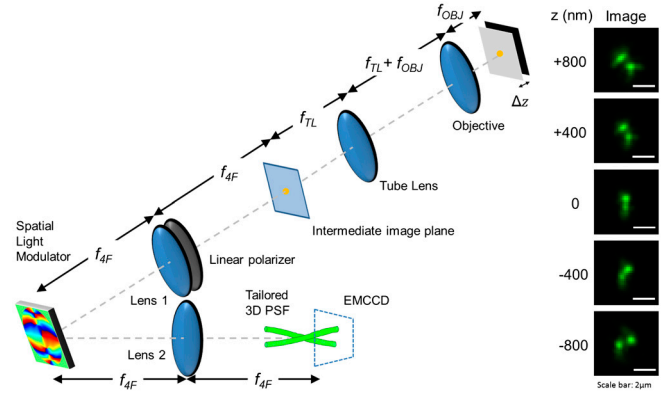
**Fig. 2.** Optical layout of PSF engineered microscope. The DH microscope collects the light emitted from the fluorescent sample. A traditional microscope with a 1.3 NA objective is appended with a 4F optical setup, used to reimage the intermediate image plane onto the detector. A spatial light modulator (SLM) is placed in the Fourier plane of the 4F setup and is used to code the optical pupil of the microscope. When the DH-PSF phase mask is present on the SLM, the light emission from the sample is encoded for subsequent imaging onto an electron-multiplying charge-coupled device, located after the second Fourier lens (Lens 2). Experimental images are given in the right pane as a nanoparticle is translated axially through focus.

$$\mathscr{L}(I_{exp}(m,n); f(m,n; \overrightarrow{o}))$$

$$= \Pi_{m=1}^{M}\Pi_{n=1}^{N} \frac{(|f(m,n; \overrightarrow{o})|^2 + b)^{I_{exp}(m,n)}}{I_{exp}(m,n)!} e^{-(|f(m,n; \overrightarrow{o})|^2 + b)} \qquad [5]$$

where the image size is $M \times N$, $(m,n)$ are indices that identify each pixel, and $b$ is a constant background noise level. To increase the per-pixel signal-to-noise ratio (SNR), the DH-PSF was sampled at one-half the Nyquist sampling rate—consistent with our experimental conditions*. To isolate the performance under the shot-noise limit, no background noise is included in the simulation results presented here. Background noise is included in the experimental results of the next section.

In Fig. 3, the MLE performance is compared for two likely scenarios along with the associated system CRLB (see *Supporting Information* for further discussion of CRLB). The first scenario characterizes the performance of the MLE algorithm when the optical pupil function was known a priori. This establishes the performance limit without introducing any potential errors from the PR algorithm. The second scenario characterizes the PR-MLE method using the PR results from the calibration images to obtain the pupil function and 3D complex-valued PSF. About 20 iterations are necessary for the MLE to converge on each estimate. We provide a measure of the estimator efficiency as $\varepsilon = \frac{\sigma_{est}}{\sigma_{CRLB}}$ —the ratio of the estimator precision (measurement standard deviation) to that of the CRLB. To develop a sense for the performance across a broad range of possible conditions, we average the efficiency of the estimator over a photon count range of 300–1,100 photons. For a system known a priori, the resulting average efficiency is $\varepsilon_{MLE,ap}(x,y,z) = (1.0 \pm 0.1, 1.0 \pm 0.1, 1.1 \pm 0.1)$ along the $x$, $y$, and $z$ directions†. Therefore, these results demonstrate that the performance of the MLE is efficient. For the PR-MLE the efficiency along the $x$, $y$, and $z$ directions is $\varepsilon_{MLE,PR}(x,y,z) = (1.0 \pm 0.1, 1.5 \pm 0.1, 1.1 \pm 0.1)$. The minor loss of precision for the PR-MLE along the $y$ coordinate

---

*Note that precise position estimation from a point response does not require full reconstruction of the signal. Further, an optimum sampling rate can be calculated for a given system and noise level (11).

†Note that an intrinsic, random error greater than 0.6 nm is associated with the estimation of $\sigma_{est}$ due to the finite distribution sample size of $N = 100$ used in the simulation. This random error is responsible for the fluctuations of $\sigma_{est}$ about the CRLB.
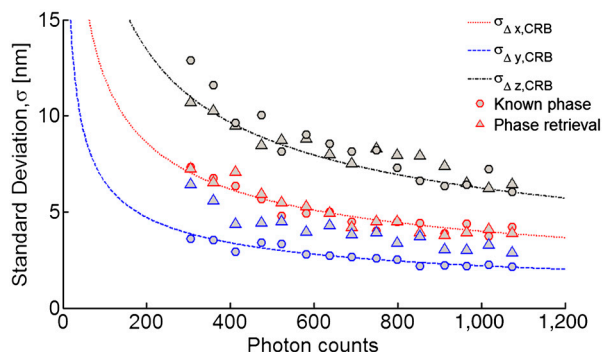
**Fig. 3.** Localization efficiency tests as measured by applying the MLE to 100 simulated, noisy images and varying the number of photon counts. The lines indicate the theoretical lower bound (CRLB) of the precision for which the x, y, and z-axis positions may be localized in the shot-noise limit with an emitter in focus ($z = 0$). The bound increases rapidly as the number of photons collected in the image decreases. The colored circles indicate the associated maximum-likelihood (ML) estimation precision when the pupil function of the optical system is well known and no PR is necessary. The colored triangles indicate the ML precision when the phase-retrieval algorithm is implemented.

is due to both the sub-Nyquist sampling conditions and the presence of noise in the calibration images used for the PR estimate. The results of Fig. 3 imply that the PR-MLE estimator is efficient in reaching the performance limit in the shot-noise-limited case (the Gaussian case including aberrations is treated in *Supporting Information*, also showing efficient estimation)

## Performance with Experimental Data

A sample of PtK1 (rat kangaroo kidney epithelial) cells expressing PA-GFP-tubulin (a photo-activatable green fluorescent protein) is examined experimentally using the DH microscope of Fig. 2 in the PALM/STORM modality (see *Supporting Information*). The axial calibration data is shown in Fig. 1*B* and the PR results are given in Fig. 1*C*. A total of 144 individual single molecules are identified in this sample under the constraint that each is present in four sequential images and yielding 998 total localization measurements. An average of $2,087 \pm 291$ photons per image was collected for this ensemble. The molecules were found to be dispersed throughout a 1.9 µm axial depth and a $25 \times 25$ µm field of view (see *Supporting Information*). The histograms in Fig. 4 show estimation results of the PR-MLE on the data-set of single-molecule measurements, each position shifted to have a mean located at the origin. Significant background is present in the experiment (an average of $349 \pm 57$

photon counts per pixel; see *Supporting Information* for background subtraction and estimation procedures). The PR-MLE estimation precision (standard deviation) on this collection of molecules along the x, y, and z directions is $\sigma_{MLE}(x,y,z) = (17,10,19)$ nm.

A sense for the experimental estimator efficiency of the PR-MLE is developed by comparison of the reported MLE precision with a representative CRLB by assuming average emitter characteristics found from the dataset (i.e., positioned at the mean axial position, emitting the average number of photons with the average background level). This CRLB is found to be $\sigma_{CRLB}(x,y,z) = (12,16,23)$ nm. The average estimator efficiency of all three position estimates is therefore 0.95, indicating that, on average, the estimator is indeed efficient at localizing experimental emitters within a volume. Note that this is only an estimate of the performance limitations for the experimental system and that the nonlinear relationship with background count levels (approximately 16% measured variation), assumptions of a uniform background, the changes of the signal level from the emitter (approximately 14% measured), as well as the averaging of performance across an extended range of axial depth, all contribute to real deviations from this CRLB estimate, which in this case, should only be taken as indicative of the expected performance of an efficient estimator. During the experiments no significant anisotropic effects were noticed due to the rotational freedom of the fluorescent proteins. If present, these anisotropies could lead to systematic errors that need to be corrected.

To illustrate the applicability of the methods presented above, we have performed distance measurement, tracking, and PALM experiments. For the distance measurement demonstration, two molecules were identified in the PALM experiment and their 3D distance measured as shown in Fig. 5. The first molecule (right-most) is localized to $\sigma_{SM1}(x,y,z) = (17,16,25)$ nm and the second molecule (left-most) is localized to $\sigma_{SM2}(x,y,z) = (9,19,20)$ nm. After propagating the random error in localization of each molecule, the distance separating them was determined as $778 \pm 22$ nm. The experimental data points are given as solid dots and each molecule position is visualized as an ellipsoid where the semiaxes are given by the respective standard deviation of each localization measurement. Tracking and PALM experiments are reported in the *Supporting Information*.

## Discussion

The experimental single-molecule localization performance compares favorably with recent 3D localization experiments in PALM/STORM. A rigorous comparison of the various experimental techniques is difficult because the available reports relate to different samples and fluorophores (10, 11, 13–15). Furthermore, 3D PALM/STORM reports do not always provide complete data (3D precision, number of detected photons, background noise level, axial range, etc.). Besides, many studies use isolated beads rather than single molecules to characterize the system's performance, which, although useful, provide favor-
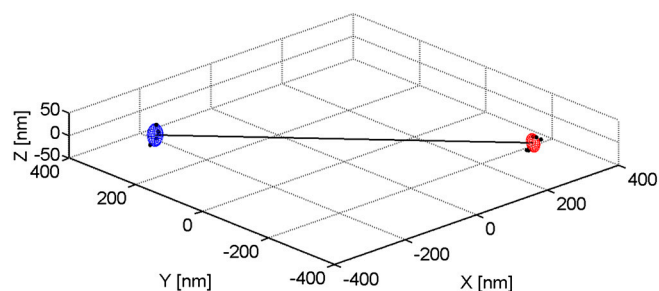


**Fig. 4.** Localization and photon counting results from 998 estimations of single-molecule positions in a PALM experiment with a DH-PSF. (*A*) The 3D scatter plot of these measurements demonstrates localization within a 17 nm × 10 nm × 19 nm volume (standard deviation). (*B*) Typical experimental image of one PA-GFP molecule (2,140 photons detected). (*C*) The distribution of counts per image reveals a normal distribution with a mean number of 2,087 photons. (*D–F*) The individual histograms of the x, y, and z-axis estimation from the ensemble used in panel *A*.



**Fig. 5.** Measurement of the distance between two PA-GFP molecules. Nine total measurements are used to localize the individual molecules. Because each molecule is well localized a high precision distance measurement can be calculated.

able detection conditions with no background noise from other emitters, no auto-fluorescence, and limited aberrations. One way around this problem is to consider fundamental assessments of the performance limits, which have recently shown the advantages of engineered PSFs (22). Another informative approach is to compare actual experimental single-molecule performances based on quantitative measures of resolution and axial range as explained in what follows.

For the shot-noise limiting case, neglecting for the moment background and pixelation noise, the localization precision follows the $1/\sqrt{N}$ scaling law (23, 34). Hence, one can use the photon-normalized geometric mean precision, $C^{3D} = \sqrt{N}\sqrt[3]{\sigma_x\sigma_y\sigma_z}$, as a resolution metric to compare 3D systems. According to this metric the system demonstrated here achieves about 50% better precision than prior 3D PALM/STORM demonstrations using astigmatic (14) and biplane (13) imaging (corresponding to approximately 3 times smaller minimum resolvable volume) with more than twice the depth range. It thus becomes closer to achieving the axial resolution of interferometric systems (10) while providing one order of magnitude longer axial range with a much simpler system (see *Supporting Information* for comparison details). It should be noted that the current DH-PSF experiment was performed with fluorescent proteins and over a long depth range, both factors that negatively affect the signal-to-background noise ratio.

The *Supporting Information* presents an experimental validation and theoretical analysis of the accuracy (bias and systematic errors) of the method, showing that with proper calibration, the procedures are faithful to represent the actual emitter positions and distances among them.

These results show that the integration of PSF engineering, photo-activation-localization imaging, and optimal estimation enables one order of magnitude improvement in resolution along each spatial direction when compared with classical fluorescence imaging. This translates into three orders of magnitude improvement in the resolvable volume over a wide 3D field of view. In addition, the unknown, systematic aberrations may be completely characterized through comparison of the PR recovered pupil and that of the expected pupil. This data may then be used to provide the user additional information concerning the sources of the aberration (e.g., spherical aberrations due to the distance from cover slip), representing a useful by-product of the method.

## Conclusion

In conclusion, the optimal estimator based on a (PR-enabled) MLE, tailored to match the conditions found in single-molecule imaging, is efficient in reaching the 3D localization performance limits with arbitrary PSFs. The rigorous depth-variant PR interpolation of calibration data takes into account systematic errors caused by unknown and unavoidable 3D optical aberrations. The optimal 3D localization algorithm in conjunction with a DH-PSF shows the best 3D localization precision in PALM/STORM systems with an extended depth range, enabling an approximately 1,000-fold improvement in resolvable volume with respect to classical fluorescence microscopy.

1. Betzig E, et al. (2006) Imaging intracellular fluorescent proteins at nanometer resolution. *Science* 313:1642–1645.
2. Rust MJ, Bates M, Zhuang X (2006) Sub-diffraction-limit imaging by stochastic optical reconstruction microscopy (STORM). *Nat Methods* 3:793–796.
3. Hess ST, Girirajan TPK, Mason MD (2006) Ultra-high resolution imaging by fluorescence photoactivation localization microscopy. *Biophys J* 91:4258–4272.
4. Egner A, et al. (2007) Fluorescence nanoscopy in whole cells by asynchronous localization of photoswitching emitters. *Biophys J* 93:3285–3290.
5. Hell SW, Wichmann J (1994) Breaking the diffraction resolution limit by stimulated emission: stimulated-emission-depletion fluorescence microscopy. *Opt Letters* 19:780–782.
6. Gustafsson MGL (2005) Nonlinear structured-illumination microscopy: Wide-field fluorescence imaging with theoretically unlimited resolution. *Proc Natl Acad Sci USA* 102:13081–13086.
7. Tang J, Akerboom J, Vaziri A, Looger LL, Shank CV (2010) Near isotropic 3D optical nanoscopy with photon limited chromophores. *Proc Natl Acad Sci USA* 107:10068–10073.
8. Pertsinidis A, Zhang Y, Chu S (2010) Subnanometre single-molecule localization, registration and distance measurements. *Nature* 466:647–651.
9. Lord SJ, et al. (2010) Azido push-pull fluorogens photoactivate to produce bright fluorescent labels. *J Phys Chem B* 114:14157–14167.
10. Shtengel G, et al. (2009) Interferometric fluorescent super-resolution microscopy resolves 3D cellular ultrastructure. *Proc Natl Acad Sci USA* 106:3125–3130.
11. Pavani SRP, DeLuca J, Piestun R (2009) Polarization sensitive, three-dimensional, single-molecule imaging of cells with a double-helix system. *Opt Express* 17:19644–19655.
12. Aguet F, Geissbuhler S, Marki I, Lasser T, Unser M (2009) Super-resolution orientation estimation and localization of fluorescent dipoles using 3-D steerable filters. *Opt Express* 17:6829–6848.
13. Juette MF, et al. (2008) Three-dimensional sub-100 nm resolution fluorescence microscopy of thick samples. *Nat Methods* 5:527–529.
14. Huang B, Wang W, Bates M, Zhuang X (2008) Three-dimensional super-resolution imaging by stochastic optical reconstruction microscopy. *Science* 319:810–813.
15. Pavani SRP, et al. (2009) Three-dimensional, single-molecule fluorescence imaging beyond the diffraction limit by using a double-helix point spread function. *Proc Natl Acad Sci USA* 106:2995–2999.
16. Pavani SRP, Piestun R (2008) Three dimensional tracking of fluorescent microparticles using a photon-limited double-helix response system. *Opt Express* 16:22048–22057.
17. Thompson MA, Lew MD, Badieirostami M, Moerner WE (2010) Localizing and tracking single nanoscale emitters in three dimensions with high spatiotemporal resolution using a double-helix point spread function. *Nano Lett* 10:211–218.
18. Thompson MA, Casolari JM, Badieirostami M, Brown PO, Moerner WE (2010) Three-dimensional tracking of single mRNS particles in *Saccharomyces cerevisiae* using a double-helix point spread function. *Proc Natl Acad Sci USA* 107:17864–17871.
19. Mlodzianoski MJ, Juette MF, Beane GL, Bewersdorf J (2009) Experimental characterization of 3D localization techniques for particle-tracking and super-resolution microscopy. *Opt Express* 17:8264–8277.
20. Pavani SRP, Piestun R (2008) High-efficiency rotating point spread functions. *Opt Express* 16:3484–3489.
21. von Middendorff C, Egner A, Giesler C, Hell SW, Schonle A (2008) Isotropic 3D nanoscopy based on single emitter switching. *Opt Express* 16:20774–20788.
22. Grover G, Pavani SRP, Piestun R (2010) Performance limits on three-dimensional particle localization in photon-limited microscopy. *Opt Letters* 35:3306–3308.
23. Ober R, Ram S, Ward ES (2004) Localization accuracy in single-molecule microscopy. *Biophys J* 86:1185–1200.
24. Kay SM (1993) *Fundamentals of Statistical Signal Processing, Volume 1: Estimation Theory* (Upper Saddle River, NJ, Prentice-Hall).
25. Aguet F, Van De Ville D, Unser M (2005) A maximum-likelihood formalism for sub-resolution axial localization of fluorescent nanoparticles. *Opt Express* 13:10503–10522.
26. Mortensen KI, Churchman LS, Spudich JA, Flyvbjerg H (2010) Optimized localization analysis for single-molecule tracking and super-resolution microscopy. *Nat Methods* 7:377–381.
27. Smith CS, Joseph N, Rieger B, Lidke KA (2010) Fast, single-molecule localization that achieves theoretically minimum uncertainty. *Nat Methods* 7:373–375.
28. Shaevitz JW, Fletcher DA (2007) Enhanced three-dimensional deconvolution microscopy using a measured depth-varying point-spread-function. *J Opt Soc Am A* 24:2622–2627.
29. Fienup JR (1982) Phase retrieval algorithms: a comparison. *Appl Optics* 21:2758–2769.
30. Hanser BM, Gustafsson MGL, Agard DA, Sedat JW (2004) Phase-retrieved pupil functions in wide-field fluorescence microscopy. *J Microsc* 216:32–48.
31. Allen LJ, Oxley MP (2001) Phase retrieval from series of images obtained by defocus variation. *Opt Commun* 199:65–75.
32. Waller L, Tian L, Barbastathis G (2010) Transport of intensity phase-amplitude imaging with higher order intensity derivatives. *Opt Express* 18:12552–12561.
33. Fienup JR (1999) Phase retrieval from undersampled broadband images. *J Opt Soc Am A* 16:1831–1837.
34. Thompson RE, Larson DR, Webb WW (2002) Precise nanometer localization analysis for individual fluorescent probes. *Biophys J* 82:2775–2783.

APPLIED PHYSICAL SCIENCES

# Supporting Information

## Quirin et al. 10.1073/pnas.1109011108

### SI Text

**The Double-Helix Point Spread Function (PSF).** The three-dimensional (3D) PSF describes the response of an optical system to a point source excitation as a function of its position in the object (sample) space. The third dimension allows for objects located out-of-focus. For volume-based imaging applications the system response to these out-of-focus objects can be determined by design (1, 2). This approach has been recently demonstrated in 3D photo-activated localization microscopy/stochastic optical reconstruction microscopy (PALM/STORM) imaging. Moving beyond a clear circular aperture, engineering the 3D shape of the PSF can expand the functionality and/or increase the sensitivity of the measurement.

The double-helix (DH) PSF is one particular example of 3D PSF that presents two lobes that rotate as the object moves out-of-focus, effectively generating a double helix in 3D space (see Figs. 1 and 2). The DH-PSF can be implemented by an amplitude/phase spatial modulation of the light at the pupil plane of the microscope. A basic implementation of the DH-PSF is realized with a proper superposition of Laguerre–Gauss modes as described in ref. 2. The design can be refined to take into account low light level situations, for instance by generating phase-only, fully transmissive masks. To first approximation, this mask can be created by simply removing the amplitude modulation of the Laguerre–Gauss mode superposition. Further efficiency improvement has been attained by use of numerical optimization (3). A numerically optimized DH-PSF phase mask is employed in this work. Refs. 1 and 3 describe in detail the procedures to calculate this type of optical element.

**Maximum-Likelihood Localization Algorithm.** The maximum-likelihood estimator (MLE) algorithm is implemented using custom software developed in the MatLab environment (The MathWorks Inc.). The operational details of the algorithm are now introduced to highlight specific contributions of the 3D phase-retrieval (PR) MLE. This section assumes the PR process is complete, and describes how to subsequently use that information for particle localization. The localization occurs in two steps: First, a coarse estimate is made to decrease the computational burden from the iterative MLE search; second, the MLE begins an iterative search for a high-precision 3D localization solution.

**Initial approximation.** The PR results can be used in the 3D search after an initial guess is made on the 3D location of the object of interest. An initial, coarse estimate is required to obtain a first approximation to the solution in the global space to reduce the complexity of the algorithm. In our case, this initial estimate is obtained in the spatial frequency domain, using the amplitude information of the experimental image and finding the closest match to the PR result at each calibration image in a sum-squared-error sense,

$$\min_{z \in [z1,...,zN]} \left\{ \sum_{m=1}^{M'} \sum_{n=1}^{N'} (|\mathcal{F}\{|f^2|\}(m,n;z)| - |\mathcal{F}\{I_{\exp}\}(m,n)|)^2 \right\},$$

[S1]

where $N$ axial calibration images separated by an axial distance $\Delta z = 100$ nm were used and the image size is $M' \times N'$. Working in the spatial frequency domain reduces the initial estimation search from three dimensions to only the axial dimension by ignoring the linear phase responsible for transverse shifts. After this initial estimate is found for the axial location, it is transversely cross-

correlated with the experimental image to find coarse $\Delta x$, $\Delta y$ coordinates.

Given this set of initial coordinates, an iterative algorithm is then implemented to find the optimum 3D coordinate in the object space $\vec{o} = \{\Delta x, \Delta y, \Delta z\}$ that maximizes the probability of matching the experimental pattern to a rigorously interpolated PSF cross-section in the presence of noise (maximum likelihood),

$$\max_{\vec{o} \in \mathbb{R}} \{\mathcal{L}(I_{\exp}(m,n); f(m,n; \vec{o}))\}$$

[S2]

**The MLE gradient-descent search.** The likelihood function ($\mathcal{L}$) can be selected to suit the appropriate imaging conditions under examination. Examples of common likelihoods include both the Poisson and Gaussian distributions,

$$\mathcal{L}(I_{\exp}(m,n); f(m,n; \vec{o})) = \prod_{m=1}^{M'} \prod_{n=1}^{N'} \frac{(|f(m,n; \vec{o})|^2)^{I_{\exp}(m,n)}}{I_{\exp}(m,n)!} e^{-|f(m,n; \vec{o})|^2}$$

[S3]

and

$$\mathcal{L}(I_{\exp}(m,n); f(m,n; \vec{o})) = \prod_{m=1}^{M'} \prod_{n=1}^{N'} \frac{1}{\sigma\sqrt{2\pi}} e^{-\frac{(I_{\exp}(m,n)-|f(m,n; \vec{o})|^2)^2}{2\sigma^2}},$$

[S4]

respectively.

Implementation of the MLE component is realized through maximization of the argument in Eq. **S2** with the following gradient-descent iterative search algorithm for each axis,

$$o_j^{(p+1)} = o_j^{(p)} - \gamma \left( \frac{\partial^2}{\partial j^2} \mathcal{L}(I_{\exp}; f(\vec{o})) \right)^{-1} \frac{\partial}{\partial j} \mathcal{L}(I_{\exp}; f(\vec{o}))|_{j=o_j^{(p)}}$$

[S5]

where $j \in \{\Delta x, \Delta y, \Delta z\}$, $p$ is the iteration number (4) and $\gamma$ is introduced to scale the search step size. Typical values for $\gamma$ ranged from $0.1 \leq \gamma \leq 1$ (0.1 was used for both the simulation and experimental results reported). Iteration is continued until the updated localization values are observed to converge. The derivatives along each axis are found numerically using central difference methods for the first-order derivative,

$$\frac{\partial}{\partial j} \mathcal{L}(I_{\exp}; f(\vec{o})) = \frac{\mathcal{L}(I_{\exp}; f(\vec{o} + \vec{h})) - \mathcal{L}(I_{\exp}; f(\vec{o} - \vec{h}))}{2|\vec{h}|}$$

[S6]

and the second-order derivative,

$$\frac{\partial^2}{\partial j^2} \mathcal{L}(I_{\exp}; f(\vec{o}))$$

$$= \frac{\mathcal{L}(I_{\exp}; f(\vec{o} + \vec{h})) - 2\mathcal{L}(I_{\exp}; f(\vec{o})) + \mathcal{L}(I_{\exp}; f(\vec{o} - \vec{h}))}{|\vec{h}|^2}$$

[S7]

where $\vec{h}$ is the displacement vector $\{h_x, h_y, h_z\}$ with nonzero values only along the direction that the derivative is taken.

**Validation of data interpolation capabilities.** Following the steps outlined in the earlier sections provides the complete algorithm for MLE implementation. To test both the quality of the PR interpolation and the MLE in the regions not bound by the constraints of a calibration image, two tests are proposed.

The first test examines the localization accuracy and precision in the axial regions between the calibration planes. The results are presented in Fig. S1*A*, showing that the PR-MLE behaves in a linear fashion between the calibration planes (the vertical shaded regions) and that the accuracy and precision are on par with that given in the calibration planes. Note that any bias present in this algorithm can be found by reference to the known calibration planes. Therefore associated calibration curves can be tabulated from the PR step and later used to correct the experimental localizations and improve accuracy.

The second test examines the precision of the PR-MLE for localization when subpixel transverse shifts of the PSF are present. In Fig. S1*B*, the results of transverse localization are given for a series of noninteger transverse shifts (integer-valued shifts are highlighted with vertical shaded regions). Again, the PR-MLE results behave both linearly and accurately with subpixel shifts in the transverse dimension. The success of these tests validate the optimality of the PR-MLE procedures highlighted above.

**Experimental Setup and Sources of Aberrations.** The experimental setup shown in Fig. 2 was used to image the photo-activatable green fluorescent protein (PA-GFP) label within a sample of kangaroo rat epithelial cell. The sample mount was attached to a piezo-driven stage (Physik Instrument P-615.3CD). A custom microscope (Zeiss objective Plan-Neo Fluar, 1.3NA) with magnification $M = 91x$ is used to image the samples. The tube lens is an achromatic lens of focal length $f_{TL} = 150$ mm. The image conjugate to the focal plane of the objective is named the intermediate image plane. This intermediate image serves as the focal plane of the 4F optical system located after the microscope stage.

For the single-molecule imaging in a biological sample, the image acquisition time was set to 500 ms. The sample was initially bleached using circularly polarized 488 nm illumination (38 mW from an Ar$^+$ laser), then reactivated with circularly polarized light from a 405-nm diode laser (0.5 mW). The reactivation illumination uses a function generator to produce a 500 ms pulse at 0.2 Hz. Each beam illuminated a 40-micron diameter field on the sample. The data was collected in an epifluorescence configuration, with a dichroic mirror placed behind the microscope objective to block/redirect the excitation/activation light and transmit about 90% of the emission from the PA-GFP. Sample prepration is described in ref. 5.

A reflective spatial light modulator (SLM, Boulder Nonlinear Systems XY-P512 SLM) is placed in the Fourier plane of the 4F system to encode the incident wave field with a double-helix PSF transfer function (3). A pair of achromatic lenses (focal length $f_{4F} = 250$ mm) and a linear polarizer make up the rest of the 4F system. The linear polarizer is utilized to select polarization parallel to the active axis of the liquid crystal modulated by the SLM and in practice was a broadband polarizing beam splitter (420–680 nm, Edmund Optics). The loss of photons in the othogonal polarization state is not necessary and has been solved with the use of additional optics (5) or with the use of phase masks (6). The final image is formed on the electron-multiplying charge-coupled device (EM-CCD) (Andor iXon), with a 16-μm pixel pitch, located a distance $f_{4F}$ behind the final 4F lens.

To maximize the light efficiency of the DH-PALM system, the light from the first Fourier lens is obliquely incident on the SLM (at 30°) so that reflected light may pass through the second Fourier lens without the use of additional beam splitters. This oblique incidence introduces aberration into the optical system from the relative loss in modulation contrast of refractive index seen by the incident light as it is modified by the SLM. Additional sources of

aberration include the use of a tilted camera in this system (5) and those inherent to volume imaging such as objectives that are optimized for imaging a single plane with minimal aberration at the cost of volume performance. Lastly, imaging sources at varying depths beyond the cover slip will be subject to spherical and specimen-induced aberrations.

**Limits of Localization and Analysis of the Cramer–Rao Lower Bound (CRLB).** The CRLB is a measure of the optical system's fundamental limit for precisely estimating a set of parameters (2), in this case, the 3D position of a particle. The CRLB provides the theoretical lower limit of the variance for any unbiased estimator in the presence of noise. It is found from the inverse of the Fisher Information, $\text{CRLB} = \text{FI}(\vec{o})^{-1}$, where

$$\text{FI}_{j,k} = \sum_{m=1}^{M} \sum_{n=1}^{N} \left\langle \frac{\partial}{\partial o_j} \ln \text{pdf}(|f(m,n;\vec{o})|^2) \frac{\partial}{\partial o_k} \ln \text{pdf}(|f(m,n;\vec{o})|^2) \right\rangle$$

[S8]

and $\{j,k\} \in \{\Delta x, \Delta y, \Delta z\}$ and pdf is the probability density function.

The CRLB for a system equivalent to the one implemented experimentally is plotted in Fig. 3. The typical range of photons detected from single molecules corresponds to the rapidly changing portion of the CRLB curve. As the photon count increases, the CRLB becomes asymptotic (7). The simulated calibration images used in the PR algorithm included Poisson noise and had a signal-to-noise ratio (SNR) of 256 (corresponding to the limit associated with a 16-bit detector).

The experimental data presented in this report was dominantly a Poisson noise process. This is verified in Fig. S2, where a typical experimental image (*A*) is analyzed to find a region of constant mean (the white region of panel *B*). The histogram of pixel photoelectron counts in this region of panel *A* is given in panel *C*, and the red curve the associated ideal Poisson distribution. The agreement between the two is an indication of the appropriateness of the noise model.

In the case of Gaussian noise and aberrations, the MLE is also verified to reach the CRLB as shown by the estimation results given in Fig. S3. This estimation was performed in the presence of spherical and coma aberrations that cause the distortion of the DH-PSF in *A* and can be seen along with the DH-PSF phase mask located in the imaging pupil (panel *B*). The MLE performance in panel *C* shows that the estimation algorithm is indeed efficient. This supports the conclusion that the presence of additional aberrations is immaterial for the MLE analysis. Indeed, the PR-MLE procedure treats any aberration or amplitude/phase modulation of a pupil plane as an aberration to be solved.

**Calibration Using Fluorescent Beads, Tracking, and Molecule Localization.** Calibration images were taken using samples prepared with 40-nm diameter fluorescent microspheres (Invitrogen yellow-green carboxylate-modified FluoSpheres). The microspheres were chosen to have similar fluorescent spectrum to the PA-GFP to minimize performance differences due to chromatic effects (excitation peak, 405 nm; emission peak, 515 nm). The 40 nm bead size is well below the diffraction limit of the microscope, therefore they were treated as point sources.

The calibration data is generated by images collected as the sample stage is translated in 100-nm intervals through the focal plane. A series of images are taken (26 is typical) at each axial location to form an average to be later used as the calibration image for PR. 2D projections of these averaged images are given as the discrete steps in Fig. 1*B*. The exposure time for each image is 273 ms and the EM-CCD is cooled to −90 °C. Using the results from the PR algorithm (the continuous 2D projection set in Fig. 1*C*), tracking of these beads was implemented with the

PR-MLE to evaluate performance. Note that the calibration data is an average at each stage position of the images used for this tracking experiment. The plot in Fig. S4 shows the estimation results corrected for bias and drift to demonstrate the precision of the MLE, the experimental depth of field, the accuracy of the estimator, and the true variability of the calibration sources. The average performance through the 2.2-μm axial range was measured to be $\sigma_{MLE}(x,y,z) = (6.6,5.0,5.2)$ nm with an average of $N_\gamma = 8{,}900$ photons collected per image.

A Poisson pdf (Eq. **5**) was utilized for the PR-MLE algorithm as justified by examination of the image noise statistics shown in Fig. S2. The histogram of experimental photo-electron counts generated in an area with approximately uniform intensity is shown to be well described by a Poisson distribution (red curve).

Individual molecules detected across four successive images, the equivelent of a 2-s duration, are used for plotting the PR-MLE results in Fig. 4. According to this definition, 144 individual molecules are identified. A total of 998 images are associated with these molecules, the positions of which are used to plot the localization precision $\sigma(x,y,z) = (17,10,19)$ nm reported in Fig. 4 *D–F*. The distribution of photon counts per image in Fig. 4*C* reports an average of $2{,}087 \pm 291$.

An individual PA-GFP molecule localization result is selected and presented in Fig. S5. This molecule is of particular interest because it stopped blinking near the end of the data acquisition cycle and therefore a long time series of images is available to analyze precision. This analysis shows that the PR-MLE localized this molecule to $\sigma_{MLE}(x,y,z) = (14,10,13)$ nm—slightly outperforming the results from the complete ensemble. Note that the relative increase in localization precision is consistent with an increase in the detected number of photons ($2{,}574 \pm 309$).

A model of the optical system that is consistent with the parameters provided above was simulated to obtain the expected CRLB when imaging individual fluorescent molecules. To obtain an estimate for the true system performance, the mean number of photons in both the signal and the background were used as calculated later in the Supporting Information (2,087 total photons and 349 photons per pixel, respectively). Using a Poisson likelihood function, given as Eq. **3**, the CRLB was calculated to be $\sigma_{CRLB}(x,y,z) = (12,16,23)$ nm. Note that this is calculated using the PR pupil so that the system aberrations are included. However, the nonoptimal estimation of the background and molecule photon counts may contribute to a skewing of the PR-MLE performance leading to localization slightly above or below the CRLB (allowed for estimators with bias).

**Depth-Variant PR Techniques.** PR can be used to determine the pupil function of an imaging system. The 3D PSF can be determined by using multiple PSF image planes for PR followed by averaging, which implies that a single optical pupil can accurately model the 3D behavior of the optical system (8, 9). This approximation requires depth invariance of the PSF and appropriately describes the behavior of low-numerical aperture (NA) systems, such as telescopes, to acceptable accuracy. In the new field of precise 3D localization with high-NA systems, the single-pupil approximation introduces errors yielding nonoptimal results. In this section we quantify the error generated by a single-pupil function model in comparison to the depth-variant model introduced in the main text.

The calibration images described above in Supporting Information are used with the PR method described in the main text to generate field estimates for each axial plane of the calibration measurements. A single optical pupil was obtained by averaging these axial estimates (taken here about the typical experimental depth of the single molecules, $-1{,}000$ nm $\leq \Delta z \leq -400$ nm) after transformation into the Fourier domain and addition of the proper phase due to propagation (see main text, Eq. **2**). According to the depth-invariant model, this single pupil suffices to represent the 3D PSF of the optical system.

The relative merit of the depth-invariant model (single-pupil function) is first compared with the depth-variant model in terms of accurately representing the rotational characteristic of the calibration images. The rotation characteristic is provided from the orientation of the two lobes relative to the camera frame of ref. 3. We follow the methods developed in ref. 3 to characterize this orientation. As a review, this method consists of finding the centroid of each of the two DH-PSF lobes and calculating their subtended angle of orientation where the origin is defined to be parallel to the y axis of the camera. Because rotation is a definitive trait of the DH-PSF, the results in Fig. S6*A* provide one measure of how well the depth-variant and depth-invariant models match the calibration data. It is seen that the depth-variant model tracks the rotational characteristic of the DH-PSF better than the depth-invariant model found from averaging the PR results.

Furthermore, to evaluate the best model for particle localization, we compare the precision obtained with each model for a single molecule. Using the same molecule analyzed with the depth-variant model earlier in the Supporting Information and plotted in Fig. S5, the precision is analyzed with a depth-invariant model for comparison. Fig. S6*B* presents the localization results of the depth-invariant model to be $\sigma_{MLE}^{DI}(x,y,z) = (16,29,21)$ nm instead of $\sigma_{MLE}^{DV}(x,y,z) = (14,10,13)$ nm, reported earlier.

**Experimental Photon Count.** To count the number of photons in a given molecule image, the spatially varying background must be accounted for. The opening image-morphology operation was utilized to analyze the image and estimate the background (10). The process is shown in Fig. S7 *A–D*, where a representative experimental image is given. Our image-opening background calculation algorithm searches the image for features that can be approximated as a collection of disk-shaped elements. By setting the size of the disk-shaped element to the dimension of a DH-PSF lobe, the DH-PSF features may be selected out, leaving only the spatially varying background in panel *B*. The morphological opening operation is implemented using the imopen command of the MatLab Image Processing Toolbox environment (The MathWorks Inc.). As a result, an accurate estimate for both the underlying, average background count and the molecule signal (panel *C*) can be made for the input to likelihood functions used in the PR-MLE. An example PR-MLE fit is presented in panel *D*.

The experimental images are collected using an electron-multiplying CCD (Andor iXon) and the number of photons incident on the detector is calculated as

$$N_\gamma = \frac{L G_{AD}}{G_{EM} \eta} \qquad \textbf{[S9]}$$

where $L$ is the ADU (analog-to-digital units) counts output from the analog-to-digital (A/D) converter, $G_{EM}$ is the electron multiplication gain (100 in our experiments), $G_{AD}$ is the number of electrons per A/D count (11.4697), and $\eta$ is the quantum efficiency of the detector (0.95 @ 515 nm).

The number of photons present in the molecule image PSF is then calculated, as shown in Fig. S7 *E–G*. Given the most-likely match from the PR-MLE, a mask is generated that represents the transverse map thresholding 80% of the intensity of the experimental PSF. The mask is applied to the background-subtracted experimental PSF for an initial photon count. This number is then scaled by the ratio of the remaining energy in an ideal PSF to the energy contained in the 80% threshold mask to estimate the total number of photons.

The background counts are found by applying the same threshold mask to the background estimate and reporting the average

number of photons per pixel within the region associated with the PSF.

**3D-DH-PALM Visualization with the Experimental Data.** The PR-MLE is performed on images from the PALM wide-field microscope dataset of the PA-GFP labeled biological sample specified in the main article. The total accumulation time was over 3.7 h. Individual molecules were selected from the image by looking for areas of high temporal variance of photon counts, indicating that a photo-activatable source has temporally fluctuated in intensity. These areas were compared with the calibration images, which serve as templates, to determine whether the local fluctuation has an intensity pattern that can be associated with the DH-PSF. If the pattern is indeed a match, the PR-MLE is implemented on this local region. A confidence measure was assigned to the estimation results according to the similarity of the estimated PSF and the experimental image. If the transverse overlap of the two patterns contained greater than 45% of the total energy, the measurement was kept. A total of 4,689 of these measurements are reported and used to plot the 3D information in Fig. S8, visualizing the volume across which the estimator performance has been demonstrated (Movie S1).

**Comparison of Reported 3D PALM/STORM Experimental Performances.** The astigmatic method (11) achieved a precision of $\sigma(x,y,z) = (9,11,22)$ nm with 6,000 photons, giving $C_{\mathrm{Astig}}^{\mathrm{3D}} = 1,004$. The optimal estimator and the experiments reported here lead to $C_{\mathrm{DH}}^{\mathrm{3D}} = 614$ and 669 for the individual single molecule and the ensemble, respectively. Note that this result was obtained with a slightly lower NA, as well as for samples with multiple emitters and lower photon counts, which increase background noise. Still this metric suggests the dramatic advantage of optimal estimators combined with tailored PSFs. Ref. 12 reports the biplane method in a PALM-like experiment with precision of $\sigma(x,y,z) = (30,30,75)$ nm and (apparently) approximately 500 photons detected, leading to $C_{\mathrm{BP}}^{\mathrm{3D}} = 910$. Ref. 13 reports resolution tested with beads of $\sigma(x,y,z) = (9.5,9.5,4.1)$ nm providing $C_{\mathrm{BP}}^{\mathrm{3D}} = 250$ but with a range of only 225 nm. For ref. 14 the values on the table are estimated; the main drawback of this method being the limited field of view in one transverse dimension (under 1 μm) as opposed to the other methods ($\gg$10 μm). This information is summarized in Table S1.

1. Piestun R, Shamir J (2002) Synthesis of three-dimensional light fields and applications. *Proc IEEE Inst Electr Electron Eng* 90:222–244.
2. Greengard A, Schechner YY, Piestun R (2006) Depth from diffracted rotation. *Opt Lett* 31:(2)181–183.
3. Pavani SRP, Piestun R (2008) High-efficiency rotating point spread functions. *Opt Express* 16:3484–3489.
4. Kay SM (1993) in *Fundamentals of Statistical Signal Processing, Volume 1: Estimation Theory*, (Prentice-Hall, Upper Saddle River, NJ).
5. Pavani SRP, DeLuca J, Piestun R (2009) Polarization sensitive, three-dimensional, single-molecule imaging of cells with a double-helix system. *Opt. Express* 17:19644–19655.
6. Grover G, Quirin S, Fiedler C, Piestun R (2011) Photon efficient double-helix PSF microscopy with application to 3D photo-activation localization imaging. *Biomed Opt Express* 2:3010–3020.
7. Ober R, Ram S, Ward ES (2004) Localization accuracy in single-molecule microscopy. *Biophys J* 86:1185–1200.

8. Hanser BM, Gustafsson MGL, Agard DA, Sedat JW (2004) Phase-retrieved pupil functions in wide-field fluorescence microscopy. *J Microsc* 216:32–48.
9. Allen LJ, Oxley MP (2001) Phase retrieval from series of images obtained by defocus variation. *Opt Commun* 199:(1–4)65–75.
10. Gonzalez RC, Woods RE, Eddins SL (2004) in *Digital Image Processing using Matlab*, (Prentice-Hall, Upper Saddle River, NJ), pp 403–420.
11. Huang B, Wang W, Bates M, Zhuang X (2008) Three-dimensional super-resolution imaging by stochastic optical reconstruction microscopy. *Science* 319:810–813.
12. Juette MF, et al. (2008) Three-dimensional sub-100 nm resolution fluorescence microscopy of thick samples. *Nat Methods* 5:527–529.
13. Shtengel G, et al. (2009) Interferometric fluorescent super-resolution microscopy resolves 3D cellular ultrastructure. *Proc Natl Acad Sci USA* 106:3125–3130.
14. Tang J, Akerboom J, Vaziri A, Looger LL, Shank CV (2010) Near isotropic 3D optical nanoscopy with photon limited chromophores. *Proc Natl Acad Sci USA* 107:10068–10073.
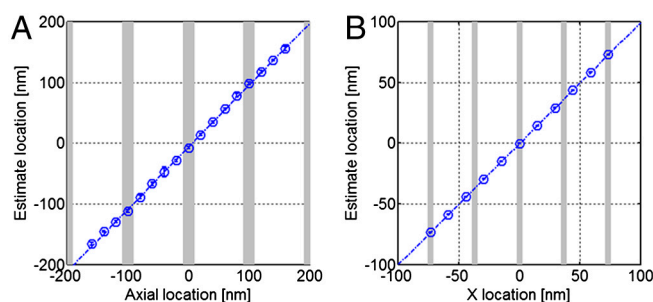
**Fig. S1.** PR-MLE results for the estimation with interpolated and subsampled 3D data. (*A*) PR-MLE results on simulated data in 20-nm intervals through ±160 nm of axial translation. The gray bands represent the axial planes where the calibration data was taken for PR. The interpolation of the PR-MLE is seen to behave linearly between the PR calibration planes, thereby demonstrating proper interpolation accuracy and precision in the axial direction. (*B*) PR-MLE results on simulated data as the source is shifted transversely in subpixel intervals. The gray bands represent integer-valued pixel shifts. The interpolation of the PR-MLE is seen to behave linearly across multiple pixels thereby demonstrating subsampled resolution in the transverse direction.



**Fig. S2.** Experimental noise characteristics. (*A*) An experimental image of a single molecule. (*B*) Image morphology returns an area of the image with near uniform background level for noise analysis (white region). (*C*) The distribution of the photo-electrons within the uniform area follows a Poisson distribution (in red).

**Fig. S3.** MLE estimation of aberrated PSFs in the presence of Gaussian noise. The experimental conditions including pupil a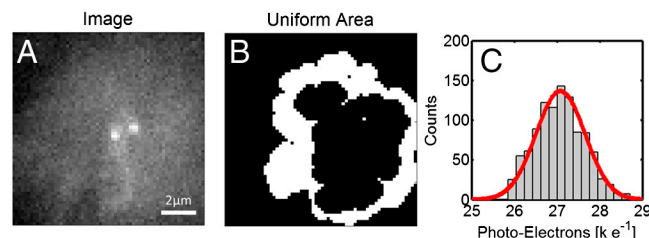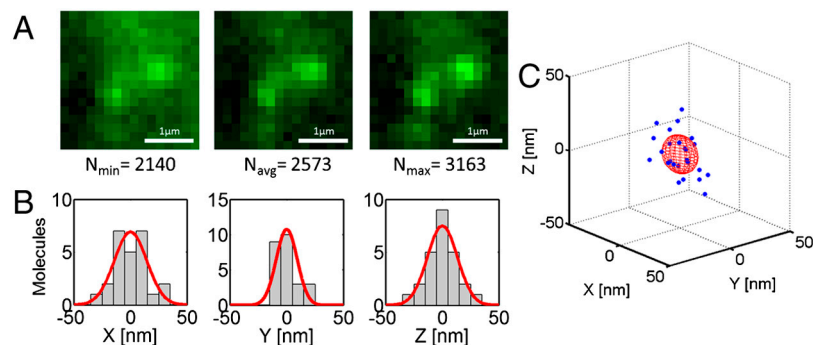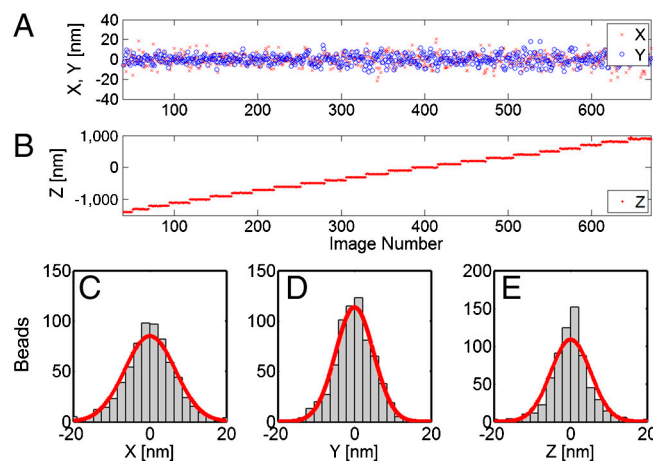berration and noise level are simulated. Results demonstrate the efficiency of the estimator for 3D localization of molecules in reaching the information theoretic limit (CRLB). (*A*) The aberrated PSF in the simulation has an asymmetric distribution of photons between the two peaks as observed in our experimental data. (*B*) The associated double-helix pupil function with coma and spherical aberrations present. (*C*) The results from the MLE estimation on 100 images (at each SNR) relative to the information theoretic Cramer–Rao Bound (CRB) lower limit when Gaussian noise is the dominant random process and the optical pupil is known as a priori (ap).



**Fig. S4.** Tracking of fluorescent beads and calibration data. The fluorescent nanoparticle calibration images are tracked in *x*, *y* (*A*), and *z* (*B*) as the piezo-electric stage is translated in 100-nm intervals. The estimation data has been corrected for bias and linear drift. The PR-MLE estimates of the complete dataset, centered about the mean for each position, are collected and shown as histograms for *x* (*C*), *y* (*D*), and *z* (*E*). The associated precision (standard deviation) for the complete dataset (671 points) through an axial range of 2.2 μm is $\sigma(x,y,z) = (6.6, 5.0, 5.2)$ nm.



**Fig. S5.** Experimental estimation performance of single-molecule localization. A single molecule is identified with an average of $2,574 \pm 309$ photons collected per image over a series of 25 images. (*A*) Representative images of the experimental data when the minimum, average, and maximum number of collected photons are present. (*B*) Histograms of the *x*, *y*, and *z* localization of the emitter, demonstrating localization precision of 14 nm, 9 nm, 13 nm, respectively. (*C*) Volume visualization of the uncertainty ellipsoid associated with the resulting estimations and the scatter of the individual measurements.
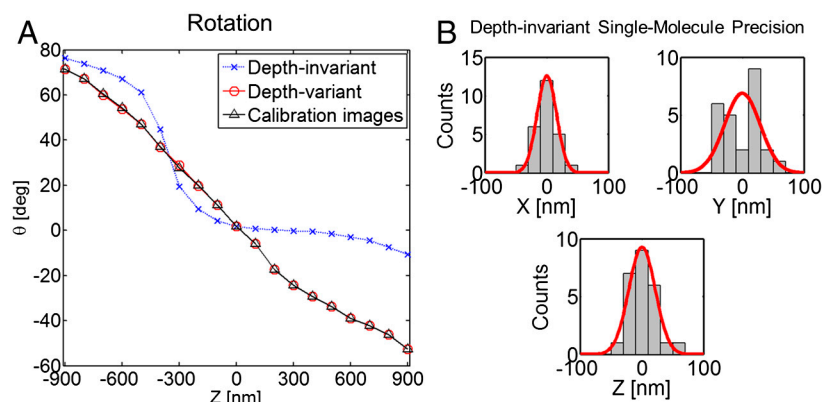
**Fig. S6.** Experimental estimation performance using a depth-invariant model in PR-MLE. (*A*) Characterizing the predicted rotation of the DH-PSF as a function of depth using the depth-invariant and depth-variant models indicates that the depth-variant model provides better agreement with the calibration data. (*B*) The depth-invariant model results in a single-molecule localization precision of 16 nm, 29 nm, 21 nm in *x*, *y* and *z*, respectively. These results are to be compared with the precision obtained using a depth-variant model shown in Fig. S5 (14 nm, 10 nm, 13 nm, respectively).
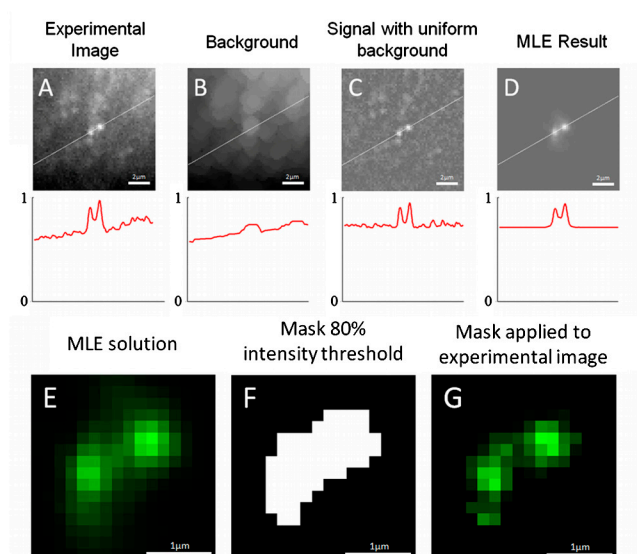


**Fig. S7.** (*A–D*) Background subtraction algorithm for experimental images. The background of the experimental single-molecule image (*A*) is estimated using an image-morphology operation with the estimated background presented in panel (*B*). The resulting background subtracted imaged (*C*) is then treated as the signal used for the PR-MLE with addition of a uniform background that is approximated as the mean value of (*B*) in the region of the DH-PSF. The result of applying the PR-MLE to this data is presented in panel (*D*). Line-outs across the DH-PSF region are given below the respective image to aid in visualizing contrast. (*E–G*) Method for counting the number of photons in an arbitrary PSF. The number of photons collected from a single molecule is quantified as the number of counts within the spatially distributed PSF. First, a most-likely solution is found using the MLE (*E*). Then a mask is generated representing the regions of the experimental image where the intensity is above threshold (panel *F*, here 80% threshold). Using the PSF returned from the PR-MLE algorithm (*E*), the remaining energy of the PSF outside this mask is calculated. The mask is applied to the background-subtracted experimental data (panel *G*) and the number of contained photon counts is scaled by the amount of energy remaining outside the mask.

**Fig. S8.** PR-MLE DH-PSF PALM imaging of rat kangaroo kidney epithelial cells expressing PA-GFP-tubulin. The distribution of a sparse set of individual molecules throughout an imaging volume is shown. Shown are 4,690 individual localization estimations, color coded according to the axial position. Molecules were found to be dispersed within a $25 \times 25 \times 1.9$ μm volume (see also Movie S1).



**Movie S1.** Three-dimensional DH-PSF PALM results showing the spatial distribution of 4690 molecule localizations.

Movie S1 (GIF)

**Table S1. Comparison of resolution and range among 3D PALM/STORM experimental results**

| 3D PALM/STORM method | Experimental resolution metric (nm)$C^{3D} = \sqrt{N} \sqrt[3]{\sigma_x \sigma_y \sigma_z}$ | Axial range (nm) | System complexity (relative to standard microscopes) |
|---|---|---|---|
| Astigmatic STORM (6) | 1,004* | 800 | Simple |
| Biplane (7) | 910* | 1000 | Simple |
| DH-PSF (this report) | 669 (ensemble)*, 614 (individual)* | 2000 | Simple |
| Interferometric (8) | 250 † | 225 | Complex |
| Virtual volume (tilted mirror) (9) | 550 † | approximately 900‡ (limited in *x* and *z*) | Simple (limited sample geometry) |

*Measured under PALM/STORM conditions with single molecules
†Measured with beads
‡Estimated value, field of view limited in one transverse coordinate